Research Square

Preprints are preliminary reports that have not undergone peer review.
They should not be considered conclusive, used to inform clinical practice,
or referenced by the media as validated information.

PIVOT: A hyper-compact, PAM-independent TIGR-Tas editor enabling efficient in vivo gene editing via AAV and LNP delivery

Yinghui Wei

yinghuiwei@nwafu.edu.cn

Northwest A&F University https://orcid.org/0000-0002-6642-1559

Kun Xu

Northwest A&F University https://orcid.org/0000-0001-5714-9090

Yufei Liu

Northwest A&F University

Panpan Wang

Northwest A&F University

Shangpu Li

Northwest A&F University

Zhenmin Wu

Northwest A&F University

Xi Cao

Northwest A&F University

Zhaoyang Mao

Northwest A&F University

Qiang Kang

Northwest A&F University

Zhe Chen

Northwest A&F University

Zijian Hu

Northwest A&F University

Ying Cao

Northwest A&F University

Yihan Qiao

Northwest A&F University

Yijun Guo

Castalysis Bioscience (Shanghai) Co., Ltd.

Rui Feng

Northwest A&F University

Yulin Chen

Northwest A&F University

Xiaolong Wang

Northwest A&F University https://orcid.org/0000-0003-1620-1344

Zhaowei Wu

Castalysis Bioscience (Shanghai) Co., Ltd.

Article

Keywords:

Posted Date: November 9th, 2026

DOI: https://doi.org/10.21203/rs.3.rs-11118113/v1

License: This work is licensed under a Creative Commons Attribution 4.0 International License.
Read Full License

Additional Declarations: There is **NO** Competing Interest.

PIVOT: A hyper-compact, PAM-independent TIGR-Tas editor enabling efficient *in vivo* gene editing via AAV and LNP delivery

Kun Xu[1,2,6*], Yufei Liu[1,6], Panpan Wang[1,2,6], Shangpu Li[1,6], Zhenmin Wu[1,2,6], Xi Cao[1,6], Zhaoyang Mao[1,3], Qiang Kang[1], Zhe Chen[1], Zijian Hu[1], Ying Cao[1], Yihan Qiao[1], Yijun Guo[3], Rui Feng[4], Yulin Chen[1,2], Xiaolong Wang[1,2*], Zhaowei Wu[3,5*], Yinghui Wei[1,2*]

[1]International Joint Agriculture Research Center for Animal Bio-Breeding of Ministry of Agriculture and Rural Affairs, College of Animal Science and Technology, Northwest A&F University, Yangling 712100, Shaanxi, China.

[2]Hainan Institute of Northwest A&F University, Sanya 572024, Hainan, China.

[3]Castalysis Bioscience (Shanghai) Co., Ltd., Shanghai 201306, China.

[4]Key Laboratory of Animal Biotechnology of the Ministry of Agriculture, College of Veterinary Medicine, Northwest A&F University, Yangling 712100, Shaanxi, China.

[5]School of Physical Science and Technology, ShanghaiTech University, Shanghai 201210, China.

[6]These authors contributed equally to this work.

[*]Corresponding authors:

xukunas@nwafu.edu.cn (K.X.), xiaolongwang@nwafu.edu.cn (X.W.),

zhaowei.wu@castalysisbio.com (Z.W.), yinghuiwei@nwafu.edu.cn (Y.W.).

Abstract

RNA-guided genome editors for therapeutic use require broad genomic access and efficient delivery, two properties that are rarely combined in existing nucleases. The compact, PAM-independent tandem interspaced guide RNA (TIGR)-Tas systems offer a promising alternative, although their editing activity remains low. Here, guided by deep mutational scanning of the TIGR-ParTasR nuclease and its cognate tigRNA, we identified that weak protein-nucleic acid contacts and intrinsic tigRNA instability are the main constraints on editing activity. Iterative engineering produced a **P**AM-**I**ndependent **V**ersatile and **O**ptimized **T**IGR-Tas editor, PIVOT, which achieves editing activity comparable to SpRY in mammalian cells with high specificity. Microinjection of the PIVOT system into mouse zygotes enabled efficient germline editing, and a single AAV vector drove durable hepatic *PCSK9* knockout, reducing circulating *PCSK9* by ~82% and serum LDL-C by ~47%. A covalently circularized tigRNA (Mobius) with enhanced RNA stability also supports efficient lipid-nanoparticle (LNP) delivery, providing a compact PIVOT/Mobius editor compatible with both AAV- and LNP-mediated *in vivo* editing.

Introduction

Programmable RNA-guided nucleases enable precise genetic modification across diverse species and have emerged as indispensable tools for biological research and therapeutic development. However, its therapeutic use is constrained by two major limitations: most RNA-guided nucleases require a protospacer-adjacent motif (PAM) or target-adjacent motif (TAM), restricting genomic accessibility[1-3]; and widely used nucleases such as Cas9 and Cas12a, along with their derivatives, generally exceed the cargo capacity of a single adeno-associated virus (AAV) vector, hampering efficient delivery to target tissues[4-6]. Split-intein and dual-vector strategies can partially overcome the size constraint, yet they introduce manufacturing complexity and reduced delivery efficiency, underscoring the need for compact, highly active editors with broad targetability that are compatible with a single AAV capsid[7-9]. Therapeutic editing of specific tissues such as skeletal muscle, retina, and central nervous system relies on AAV-mediated *in vivo* delivery, and minimizing editor size is therefore a central objective for *in vivo* genome-editing therapeutics.

Efforts to overcome these limitations have followed two routes. Miniature nucleases, including Cas12f, Cas12j, IscB, TnpB, and Fanzor[10-22], are sufficiently compact for viral

delivery, but most retain PAM or TAM requirements and demand extensive protein and guide RNA engineering to achieve robust activity in mammalian cells. Conversely, near-PAM-less Cas9 variants, such as SpRY[23-26] and its derivatives, have overcome this constraint through mutagenesis of the PAM-interacting domain, enabling editing at virtually any genomic locus. Their large size, however, precludes packaging into a single AAV vector.

The recently discovered tandem interspaced guide RNA array (TIGR) and TIGR-associated protein (Tas) systems are a distinct class of compact RNA-guided nucleases that may address this gap[27]. The TIGR arrays are processed into short dual-spacer tigRNAs, which direct DNA recognition via a tandem-spacer mechanism that contrasts with the single-guide RNA architecture of CRISPR-Cas. The compact TasR nuclease (~340 amino acids) comprises a Nop domain homologous to the guide-binding core of archaeal box C/D small nucleolar ribonucleoproteins (snoRNPs) and assembles into a C2-symmetric dimer through its C-terminal coiled-coil domain. The dimer recognizes target DNA with no apparent PAM requirement and cleaves it via two RuvC domains, generating staggered double-strand breaks[27]. Structural studies of the related TasH nuclease have further elucidated how dual-spacer tigRNAs mediate PAM-independent target recognition and DNA cleavage[28,29]. Wild-type TasR orthologs, however, exhibit low editing activity in mammalian cells, and the determinants of this deficiency remain unclear[27].

In this study, we systematically dissect the molecular determinants of TIGR-TasR editing activity by deep mutational scanning of thousands of ParTasR and tigRNA variants at single-residue or single-nucleotide resolution, generating quantitative sequence–function landscapes that define key protein-RNA-DNA contacts. Through DMS-guided combinatorial engineering of ParTasR and its cognate tigRNA, we generated a **P**AM-**I**ndependent **V**ersatile and **O**ptimized **T**IGR-Tas editor, termed **PIVOT**, which exhibits substantially enhanced genome-editing activity in mammalian cells. We further demonstrate its versatility *in vivo*: microinjection of ParTasR-mRNA and tigRNA enabled efficient germline editing in mouse zygotes, and single-AAV delivery achieved robust hepatic *PCSK9* knockout, resulting in marked serum LDL-C reduction. Taking advantage of the intrinsic symmetry of the TasR–tigRNA complex, we engineered a circular tigRNA variant, termed **Mobius**, that enhances RNA stability and *in vivo* editing activity. Together, these results establish **PIVOT/Mobius** as a system that combines single-AAV packaging, broad genomic accessibility, and high editing activity—properties that are essential for *in vivo* therapeutic genome editing.

Results

Deep mutational scanning defines the ParTasR fitness landscape

To identify determinants limiting ParTasR editing activity, we performed deep mutational scanning (DMS) of full-length ParTasR in *Escherichia coli* using a cleavage-dependent *ccdB* counterselection assay (Fig. 1a). Active ParTasR variants cleave the *ccdB*-containing plasmid, thereby permitting cell survival under selection. Deep sequencing of three independent screens yielded highly reproducible enrichment profiles across thousands of variants (Fig. 1b,c and Supplementary Fig. 1). Next, we evaluated 125 single-amino-acid substitutions exhibiting significant enrichment with a mean $\log_2$ fold change above 1.0 relative to wild-type ParTasR (Fig. 1c). These gain-of-function mutations clustered in the RNA-binding domain (n = 83), the RuvC nuclease domain (n = 24), and the coiled-coil (CC) dimerization domain (n = 18), whereas most substitutions in the C-terminal loop were neutral (Fig. 1c,d). Projecting enrichment scores onto an AlphaFold3-predicted ParTasR-tigRNA-DNA ternary complex revealed that hyperactive hotspots cluster predominantly on nucleic-acid-binding interfaces, proximal to tigRNA or DNA (Fig. 1e). This spatial distribution indicates that suboptimal protein-nucleic-acid interactions are the primary bottleneck limiting wild-type ParTasR activity, and the DMS-identified hyperactive substitutions thus provides a roadmap for engineering improved TIGR-Tas editors by strengthening contacts with tigRNA or DNA.

From fitness landscape to a hyperactive engineered TIGR-Tas editor

Leveraging this fitness landscape, we systematically evaluated the editing activities of these 125 variants in mammalian cells. The ten top-performing substitutions, E217W/F/Y, Q239F/W, L256R, D276Q/H, and S280K/R, converged on five hotspots within the RBD, conferring a 2.53- to 3.53-fold higher editing activity than wild-type ParTasR (Fig. 2a,b). These substitutions enhance activity via two distinct biophysical mechanisms that both strengthen ParTasR-nucleic-acid contacts and stabilize the active targeting complex. The first class introduces *de novo* π-π stacking with target-DNA nucleobases: aromatic substitutions E217W/F/Y and Q239F/W stack with dG8 and dA19, respectively, stabilizing DNA binding (Fig. 2c). The second class comprises basic and polar substitutions whose extended side chains establish additional hydrogen-bonding and electrostatic contacts with the phosphate backbone and nucleobases. L256R and D276Q/H project their side chains toward the phosphate groups of dA4 and dG6, respectively, forming new hydrogen bonds that stabilize DNA binding. S280K/R instead extend long cationic side chains toward the nucleobase of

rA23 in tigRNA, reinforcing ParTasR-tigRNA assembly through additional hydrogen bonds (Fig. 2c). Together, these data implicate suboptimal protein-nucleic-acid contacts as the principal factor limiting ParTasR-tigRNA activity. ParTasR is smaller than most RNA-guided nucleases even as a homodimer, and its tigRNA lacks the stable stem-loops that anchor sgRNAs or crRNAs to their CRISPR effectors. Accordingly, targeted substitutions at the protein-nucleic-acid interface substantially improve editing activity, establishing interface engineering as a rational strategy for this compact system.

To further improve ParTasR activity, we combined the ten top single substitutions in pairwise combinations and evaluated them at the *CXCR4* locus in mammalian cells. These double mutants revealed predominantly additive-to-synergistic interactions, with most exceeding the activity of either parent (Fig. 2d). The strongest combinations, E217F/Q239F and E217W/S280R, which bridge contacts to both tigRNA and DNA, achieved ~6-fold improvement over the wild-type ParTasR. We extended this strategy to higher-order combinations, systematically screening triple, quadruple, and quintuple mutants at *CXCR4* and *B2M* (Fig. 2e). The best combinations reached ~13-fold higher activity than wild-type, indicating that individual interface contacts can be stacked with little or no epistatic penalty. To rigorously compare the leading combinatorial variants, we performed dose-response profiling across a broad mRNA dose range at human *CXCR4* and mouse *PCSK9* (Fig. 2f,g). The triple mutant p3.5 (E217W/L256R/S280R) outperformed all other combinations and achieved the highest editing activity. Together, these results show that the protein–nucleic-acid interface is a tunable engineering target, and that strengthening these contacts can enhance compact RNA-guided genome editors.

TigRNA structural engineering boosts ParTasR activity

Unlike CRISPR guide RNAs, which fold into stable stem-loops that are bound and protected by their effectors, the tigRNA is remarkably short (~36 nt) and lacks stable secondary structure. Its 5’ and 3’ termini lie only 4~5 nt from the spacer sequences, leaving them vulnerable to exonucleolytic degradation and potentially limiting editing activity (Fig. 3a). We therefore generated saturation libraries for each tigRNA structural element—central loop, boxC/boxD motifs, and terminal edges — and screened them with the same *ccdB* counterselection assay.

Deep sequencing of three independent screens produced reproducible enrichment profiles across thousands of tigRNA variants, suggesting the screen was working reliably

(Supplementary Fig. 2). We first screened saturated mutagenesis libraries with single or consecutive double-nucleotide insertions, deletions and substitutions across the tigRNA scaffold, but none gave a $Log_2FC > 1$, suggesting the scaffold is tightly constrained (Supplementary Fig. 3). We next dissected the central loop connecting the boxC/boxD elements at loop lengths of 4, 5, and 6 nt. Most variants in these libraries were deleterious, and only a few 6-nt loop sequences improved the activity ($Log_2FC > 1$, Fig. 3b and Supplementary Fig. 4). We chemically synthesized these hits and tested them in mammalian cells, and only two—Loop_AAUAUA (r1.2) and Loop_UCAUGU (r1.4)—improved editing activity, by 8.60- and 5.02-fold, respectively (Fig. 3c). The AlphaFold3-predicted structure of the ParTasR-tigRNA-DNA complex offers a structural explanation for this sequence essentiality. The native 4-nt loop does not match any canonical stable tetraloop sequence, but it engages ParTasR in a well-defined interaction network: rA18 forms van der Waals interactions with Y316; S195, the S194 pair, and T312 hydrogen-bond to the rA17 backbone, rA18 backbone, and rA18 base, respectively; while rA17, rA19, rC20 and rC21 form an intramolecular van der Waals network that gives the loop some self-folding ability (Fig. 3d). So the central loop serves both as a self-folding unit and a protein anchor, which is why most loop mutations are poorly tolerated. Moreover, saturated mutagenesis of the box C/D motifs confirmed the functional importance of these ancestral snoRNA-like elements, with most single nucleotide substitutions being deleterious (Fig. 3e). The nucleotides in the box C/D motifs interact extensively with ParTasR, consistent with the previously reported structure of TaTasR[27] (Fig. 3f). Only a few substitutions improved editing activity, with boxC_UAC/boxD_AA (r2.3) giving a 4.26-fold increase (Fig. 3g).

In prime editing, appending structured RNA motifs to the 3' end of pegRNAs improves their stability and editing efficiency. We therefore tried to stabilize the short tigRNA by appending a panel of known stabilizing motifs (5'-PH, 3'-PH, BoxB, MS2, XRN1, mpknot-1, evopreq1-1, HS, ERC1, TNS1, NRAS, TERRA, MT3, hTR, Seq1, aptamer1, and aptamer2) to its 5' and 3' ends, and in parallel by extending the terminal with a paired-stem library of 2~5 bp (Fig. 3h,i and Supplementary Fig. 5). Screening showed that most appended RNA motifs and terminal stems longer than 4 bp enhanced activity (Fig. 3h,i and Supplementary Fig. 5). The optimized variant r3.13, incorporating a terminal ACAUC-GAUGU stem, increased editing activity by 17.04-fold in mammalian cells (Fig. 3j). Dose-response profiling showed that the engineered variants outperformed wild-type tigRNA across all concentrations, with r3.13 giving the highest editing activity (Fig. 3k). Together, these results suggest that

rapid intracellular degradation represents a second bottleneck for the system, and that stabilizing the terminal stem extends tigRNA half-life and improves editing.

Engineered PIVOT rivals SpRY in activity and specificity

After optimizing both ParTasR and tigRNA variants, we paired ParTasR-p3.5 with tigRNA-r3.13 to generate PIVOT (**P**AM-**I**ndependent **V**ersatile and **O**ptimized **T**IGR-Tas editor), and benchmarked it against wild-type ParTasR and SpRY—a near-PAM-less Cas9 variant with comparable targeting scope (Fig. 4a). Across 24 endogenous targets spanning six loci (*TTR*, *CXCR4*, *SOCS1*, *B2M*, *BCL11A*, and *VEGFA*), PIVOT outperformed wild-type ParTasR at all tested loci, with indel frequencies comparable to those of SpRY (Fig. 4b,c). We next assessed whether the enhanced activity compromises targeting fidelity. Off-target profiling at four representative sites showed that PIVOT retained high on-target editing while most predicted off-target sites remained at background levels (Fig. 4d and Supplementary Fig. 6). Sporadic off-target events were comparable to wild-type ParTasR in both number and level, and were fewer than those seen with SpRY (Fig. 4d and Supplementary Fig. 6). Together, these data show that the compact PIVOT editor combines near-PAMless targeting with high fidelity, supporting its further development for therapeutic genome editing.

PIVOT enables efficient AAV-mediated *in vivo* genome editing

Targeting eight sites in the mouse *PSCK9* (a therapeutic target for familial hypercholesterolemia) gene with PIVOT to induce frameshift mutations in cultured N2a cells, we identified target2 (47.1%) with relatively high editing efficiency for subsequent experiments (Supplementary Fig. 7a). We next tested PIVOT *in vivo* by injecting ParTasR-p3.5 mRNA and tigRNA-r3.13 (targeting *PCSK9*) into mouse zygotes (Fig. 5a). No significant difference in blastocyst development rate was observed between the PIVOT-targeted groups (target 2) and the control group (Supplementary Fig. 7b). The edited pups had efficient gene knockout, with median and mean indel frequencies of 60.3% and 51.0% (Fig. 5b and Supplementary Fig. 8), along with ~85% reductions in serum PCSK9 protein and ~50% in LDL cholesterol (LDL-C) relative to controls (Fig. 5c,d). We subsequently evaluated PIVOT *in vivo* for therapeutic potential using a single AAV8 vector. After tail-vein injection into C57BL/6 mice at 5×10^{13} vg/kg, circulating PCSK9 decreased progressively and remained low, reaching ~82.0% relative to AAV8-EGFP controls by day 63, with ~25.4% indels in bulk liver (Fig. 5e-h). Consistent with *PCSK9* knockout, hepatic PCSK9 immunostaining was nearly absent in AAV8-PIVOT-treated mice, and serum LDL-C was

reduced by ~47.0% relative to AAV8-EGFP controls (Fig. 5i-k and Supplementary Fig. 9). These results demonstrate that PIVOT can achieve therapeutic-level genome editing in mice.

Circular tigRNA boosts activity and enables non-viral *in vivo* genome editing

The ParTasR-tigRNA-DNA complex is homodimeric and symmetric. We reasoned that circularizing the tigRNA would remove its exonuclease-sensitive ends and creat a symmetric, continuous scaffold that might promote RNP assembly moe effectively than the linear guide. We therefore synthesized covalently closed circular tigRNAs with symmetric central loops and called them Mobius (Fig. 5l). Dose-response profiling showed that Mobius V1 (symmetric loops) outperformed Mobius V2 (asymmetric) and all linear tigRNAs, suggesting that symmetry helps ParTasR-tigRNA assembly (Fig. 5l). The terminal-stem variant r3.13 matched the stabilizing effect of chemical modifications (2'-O-methyl and phosphorothioate, Mod V2), suggesting that degradation at the termini limits TIGR-ParTasR activity (Fig. 5l). We then evaluated PIVOT and PIVOT/Mobius for *in vivo* genome-editing activity in mice following LNP delivery (Fig. 5m). Circular Mobius V1 outperformed PIVOT with linear tigRNA across all doses (1.5-2.7 mpk), reaching a mean indel frequency of 18.2% at the highest dose (Fig. 5n). The dose-response profile mirrored the cellular results and narrowed the gap to SpRY. Together, these results show that covalently closed Mobius tigRNAs overcome terminal degradation and support robust *in vivo* editing approaching SpRY levels, providing a versatile platform compatible with both AAV and LNP delivery.

Discussion

Current genome editors usually force a trade-off between activity, targeting scope and deliverability. Near-PAM-less Cas9 variants like SpRY offer broad targeting but are too big for a single AAV, whereas miniature nucleases fit the vector yet are PAM-restricted and require extensive engineering for therapeutic potency. The TIGR-TasR system described here addresses this trade-off by combining compact size with broad targeting and potent activity. Through deep mutational scanning and mechanism-guided engineering, we overcame two major bottlenecks limiting the ParTasR system—suboptimal protein-nucleic-acid interactions and tigRNA instability. The resulting PIVOT is a ~340-aa editor that matches SpRY in activity across various endogenous loci and is fully compatible with both AAV and LNP delivery.

The suboptimal protein-nucleic-acid interactions identified by DMS were enhanced via two distinct biophysical mechanisms: (i) aromatic substitutions that establish novel π-π

stacking with DNA nucleobases, and (ii) basic or polar substitutions that introduce additional hydrogen-bonding and electrostatic contacts with the phosphate backbones of tigRNA and DNA. Similar mechanisms have been reported in the engineering of hyperactive Cas12f, TnpB, and Fanzor nucleases[10,11,16,17,30]. Cas12f, however, forms an asymmetric homodimer in which the two identical subunits play distinct structural roles[31]. This asymmetry means that a given substitution can affect each monomer differently, limiting combinatorial options and requiring residue-level optimization. In contrast, TasR forms a symmetric homodimer that ensures identical beneficial substitutions act uniformly across both monomers. Consequently, a single mutation provides a duplicated benefit—an architectural advantage over compact CRISPR or CRISPR-like systems. This symmetry likely explains the additive and synergistic effects of combining these substitutions, with the triple mutant p3.5 (E217W/L256R/S280R) achieving up to a ~9.1-fold improvement in editing activity.

Unlike CRISPR guide RNAs, whose stable stem-loops are bound and protected by their cognate effectors, the 36-nt tigRNA lacks stable secondary structure, leaving its 5' and 3' ends exposed to exonucleases. A systematic screen for terminal extensions identified r3.13, which enhances the edge duplex via a terminal ACAUC-GAUGU stem-loop. This architecture gave protection comparable to 2'-O-methyl and phosphorothioate modifications, boosting editing activity by up to ~17-fold. These findings generalize the RNA-stabilization paradigm established for pegRNAs, in which 3'-end degradation compromises prime editing, whereas structured motifs like MS2 and MT3 can restore efficiency[32-35]. Circularization protects against exonuclease degradation and has improved editing in Cas12a, Cas13d, and Cas12f systems[36-38]. However, current designs depend on ribozyme-ligase processing or exogenous linkers, which add bulk and can distort the guide structure. Mobius tigRNA gets around these issues by taking advantage of the TasR-tigRNA complex's intrinsic symmetry. The boxC/boxD architecture positions the native 5' and 3' termini within the symmetric dimer, permitting covalent closure without extraneous sequences. This design eliminates exonuclease-vulnerable ends and creates a new symmetric central loop that serves as an additional protein-binding interface. In line with this design, the symmetric Mobius V1 variant outperforms both asymmetric and linear guides in cells and *in vivo*.

The engineered **P**AM-**I**ndependent **V**ersatile and **O**ptimized **T**IGR-Tas editor (**PIVOT**) editor showed robust *in vivo* activity when delivered as mRNA, AAV, or LNP. Microinjection of mRNA and tigRNA achieved robust germline editing in mouse zygotes, reducing serum PCSK9 by ~80% and LDL-C by ~50% in edited mouse pups. A single AAV8

vector mediated significant hepatic PCSK9 knockout and LDL-C reduction in adult mice. LNP-delivered PIVOT/Mobius achieved SpRY-like potency while retaining high specificity. In contrast to existing platforms which often compromise on one critical dimension, such as SpRY's large size, CasMINI's restricted targeting range, or the low activity of other unengineered compact systems. The PIVOT/Mobius systems uniquely reconciles broad genomic accessibility, SpRY-comparable efficiency, high specificity, and delivery versatility using AAV and LNP. Beyond genome editing, the TIGR-Tas platform has also been repurposed for ultra-compact, multiplexed programmable gene activation. The resulting TIGRa activator—less than half the size of dSpCas9-based counterparts—can activate up to 12 endogenous genes from a single construct, illustrating the platform's versatility in both genome editing and gene regulation[39].

References

1. Zhang, F. & Huang, Z. Mechanistic insights into the versatile class II CRISPR toolbox. *Trends Biochem. Sci.* **47**, 433–450 (2022).
2. Collias, D. & Beisel, C.L. CRISPR technologies and the search for the PAM-free nuclease. *Nat. Commun.* **12**, 555 (2021).
3. Nishimasu, H. et al. Structural Basis for the Altered PAM Recognition by Engineered CRISPR-Cpf1. *Mol. Cell* **67**, 139–147.e132 (2017).
4. Bak, R.O. & Porteus, M.H. CRISPR-Mediated Integration of Large Gene Cassettes Using AAV Donor Vectors. *Cell Rep.* **20**, 750–756 (2017).
5. Kong, X., Li, T. & Yang, H. AAV-mediated gene therapies by miniature gene editing tools. *Sci. China Life Sci.* **67**, 2540–2553 (2024).
6. Pedrazzoli, E. et al. CoCas9 is a compact nuclease from the human microbiome for efficient and precise genome editing. *Nat. Commun.* **15**, 3478 (2024).
7. Gao, Z. et al. A truncated reverse transcriptase enhances prime editing by split AAV vectors. *Mol. Ther.* **30**, 2942–2951 (2022).
8. Riedmayr, L.M. et al. mRNA trans-splicing dual AAV vectors for (epi)genome editing and gene therapy. *Nat. Commun.* **14**, 6578 (2023).
9. Nakane, T. et al. Structure and engineering of Cas9. *Commun. Biol.* **7**, 803 (2024).
10. Wei, Y. et al. Engineering eukaryotic transposon-encoded Fanzor2 system for genome editing in mammals. *Nat. Chem. Biol.* **22**, 48–57 (2026).

11. Li, S. et al. Engineering the MmeFz2-ωRNA system for efficient genome editing through an integrated computational-experimental framework. *Nat. Commun.* **17**, 1867 (2026).
12. Wu, Z. et al. Programmed genome editing by a miniature CRISPR-Cas12f nuclease. *Nat. Chem. Biol.* **17**, 1132–1138 (2021).
13. Kannan, S. et al. Evolution-guided protein design of IscB for persistent epigenome editing in vivo. *Nat. Biotechnol.* **44**, 759–770 (2026).
14. Thornton, B.W. et al. Engineered TnpB genome editors for plants and human cells identified by ribonucleoprotein mutational scanning. *Nat. Biotechnol.* (2026).
15. Saito, M. et al. Fanzor is a eukaryotic programmable RNA-guided endonuclease. *Nature* **620**, 660–668 (2023).
16. Skopintsev, P. et al. Structure and evolution-guided design of minimal RNA-guided nucleases. *Science* **393**, 313–318 (2026).
17. Su, M. et al. Molecular basis and engineering of miniature Cas12f with C-rich PAM specificity. *Nat. Chem. Biol.* **20**, 180–189 (2024).
18. Park, S.J. et al. Robust genome editing activity and the applications of enhanced miniature CRISPR-Cas12f1. *Nat. Commun.* **16**, 677 (2025).
19. Ma, S. et al. hpCasMINI: An engineered hypercompact CRISPR-Cas12f system with boosted gene editing activity. *Nat. Commun.* **16**, 5001 (2025).
20. Wang, Y. et al. A highly specific CRISPR-Cas12j nuclease enables allele- specific genome editing. *Sci. Adv.* **9**, eabo6405 (2023).
21. Altae-Tran, H. et al. The widespread IS200/IS605 transposon family encodes diverse programmable RNA-guided endonucleases. *Science* **374**, 57–65 (2021).
22. Karvelis, T. et al. Transposon-associated TnpB is a programmable RNA-guided DNA endonuclease. *Nature* **599**, 692–696 (2021).
23. Christie, K.A. et al. Precise DNA cleavage using CRISPR-SpRYgests. *Nat. Biotechnol.* **41**, 409–416 (2023).
24. Walton, R.T., Christie, K.A., Whittaker, M.N. & Kleinstiver, B.P. Unconstrained genome targeting with near-PAMless engineered CRISPR-Cas9 variants. *Science* **368**, 290–296 (2020).
25. Ren, Q. et al. PAM-less plant genome editing using a CRISPR-SpRY toolbox. *Nat. Plants* **7**, 25–33 (2021).
26. Zhang, W. et al. In-depth assessment of the PAM compatibility and editing activities of Cas9 variants. *Nucleic Acids Res.* **49**, 8785–8795 (2021).

27. Faure, G. et al. TIGR-Tas: A family of modular RNA-guided DNA-targeting systems in prokaryotes and their viruses. *Science* **388**, eadv9789 (2025).
28. Yang, J. et al. Molecular basis for dual-spacer-guided target cleavage by the TIGR-TasH system. *Mol. Cell* **86**, 1217-1229 (2026).
29. Zhou, R. et al. Molecular basis of single-mismatch-induced nuclease-to-nickase conversion in TIGR-TasH. *Nucleic Acids Res.* **54**, gkag743 (2026).
30. Xu, P. et al. Structural insights into the diversity and DNA cleavage mechanism of Fanzor. *Cell* **187**, 5238–5252.e5220 (2024).
31. Guan, K. et al. Comparative characterization of Cas12f orthologs reveals mechanistic features underlying enhanced genome editing efficiency. *Nat. Struct. Mol. Biol.* **33**, 756–767 (2026).
32. Nelson, J.W. et al. Engineered pegRNAs improve prime editing efficiency. *Nat. Biotechnol.* **40**, 402–410 (2022).
33. Zhang, G. et al. Enhancement of prime editing via xrRNA motif-joined pegRNA. *Nat. Commun.* **13**, 1856 (2022).
34. Lu, Y. et al. Two Highly Efficient Prime Editing Systems Based on the Csy4 CRISPR Endonuclease. *Plant Biotechnol. J.* **24**, 828–830 (2026).
35. Sakai, H.A. et al. Directed evolution of small RNA-stabilizing motifs that improve prime-editing efficiency. *Nat. Biotechnol.* (2026).
36. Zhang, X. et al. Engineered circular guide RNAs boost CRISPR/Cas12a-and CRISPR/Cas13d-based DNA and RNA editing. *Genome Biol.* **24**, 145 (2023).
37. Wang, J. et al. Enhancement of CRISPR-Cas12a system through universal circular RNA design. *Cell Reports Methods* **5**, 101076 (2025).
38. Zhang, X. et al. Engineered circular guide RNAs enhance miniature CRISPR/Cas12f-based gene activation and adenine base editing. *Nat. Commun.* **16**, 3016 (2025).
39. Liu, Z. et al. TIGRa: An ultra-compact programmable activator enabling multiplexed and efficient gene regulation. *Cell Stem Cell*, **33**,1553-1566.e4 (2026).

Methods

Deep mutational library construction and screening

To map sequence–function relationships of ParTasR, we constructed a deep mutational scanning (DMS) library covering all single-amino-acid substitutions. The ParTasR coding sequence, codon-optimized for expression in *Escherichia coli*, was divided into seven contiguous segments of approximately 150 bp. Oligonucleotides encoding saturated single-amino-acid substitutions, flanked by primer-binding sites and homology arms for Gibson assembly, were synthesized by Twist Bioscience. The tigRNA scaffold DMS library comprised five sublibraries, each targeting a distinct structural element. The first sublibrary contained single-nucleotide and consecutive double-nucleotide insertions, deletions and substitutions across the entire scaffold. The second sublibrary comprised saturation mutagenesis of central loops of 4–6 nt in length. The third sublibrary randomized the conserved box C/D motifs at both ends of the tigRNA. The fourth sublibrary extended the edge1–edge2 duplex by introducing paired stems of 2–5 nt in length. The fifth sublibrary appended 17 known structured RNA motifs to the termini of the tigRNA. Together, the five sublibraries comprised 10,148 variants, which were synthesized by Twist Bioscience as pooled oligonucleotide libraries containing flanking primer-binding sites and homology arms for Gibson assembly. These sublibraries were individually PCR-amplified, assembled into the corresponding linearized vectors, and electroporated into *E. coli*. Library plasmids were extracted to yield seven ParTasR DMS sublibraries and five tigRNA DMS sublibraries. For selection, an arabinose-inducible *ccdB* toxin plasmid was first transformed into *E. coli* Top10. Each DMS sublibrary was then electroporated into this strain for selection. Variant regions were PCR-amplified and sequenced on an Illumina NovaSeq 6000 platform. For each variant, enrichment was calculated as the fold change (FC) in read frequency between the selection and non-selection conditions, normalized to the corresponding FC of wild-type ParTasR or tigRNA.

Structure prediction by AlphaFold3

The ParTasR-tigRNA-DNA complex structure was predicted using the AlphaFold3 web server with default parameters[40]. The inputs consisted of two copies of full-length ParTasR, the cognate tigRNA and a 38-bp double-stranded DNA target containing the protospacer. The resulting model was refined and manually adjusted in Coot[41] against the related TasR complex structure (PDB: 9MTY)[27], which served as a reference for nucleic acid topology and

base-pairing register. Structural figures were prepared using UCSF ChimeraX[42].

Plasmid vector construction

Plasmids were cloned using standard molecular cloning techniques. Human codon-optimized wild-type ParTasR and tiRNA scaffold were synthesized by HuaGene Co. Ltd. For ParTasR-tiRNA plasmid construction, Phanta UniFi Master Mix (Vazyme) was used for PCR, and the Basic Seamless Cloning and Assembly Kit (TransGen) for fragment assembly. Each plasmid includes a CMV enhancer, chicken β-actin promoter, 3×FLAG, SV40 NLS, ParTasR protein, nucleoplasmin NLS, bGH poly(A) signal, U6 promoter, and tiRNA in sequence. The tiRNA target oligonucleotides were ordered from Tsingke Biotechnology Co. Ltd, annealed and ligated into BsaI digested backbone vectors using T4 DNA Ligase (Thermo Fisher Scientific). ParTasR mutants and tigRNA variants with efficient genome-editing activity are listed in Supplementary Tables 1 and 2.

Cell culture, transfection, and flow cytometry analysis

Human HEK293T and mouse N2a cells were maintained in Dulbecco's modified Eagle medium (DMEM; Corning) supplemented with 10% fetal bovine serum (FBS; Excell) and 1% penicillin–streptomycin at 37 °C with 5% CO_2. Mycoplasma testing was performed bimonthly using a commercial detection kit (Vazyme). For plasmid delivery, cells were seeded in 24-well plates at 1.0×10^5 cells per well and transfected at approximately 80% confluency with 750 ng of a single plasmid encoding ParTasR and its cognate tigRNA, using polyethylenimine (PEI) at a 1:2 DNA-to-PEI ratio (w/w). At 72 h post-transfection, mCherry-positive cells were isolated by fluorescence-activated cell sorting (FACS) using a BD FACSAria III (Supplementary Fig. 10). For RNA delivery, cells were seeded in 48-well plates at 4.0×10^4 cells per well and transfected 24 h later with 250 ng of ParTasR mRNA and 500 ng of tigRNA using 0.5 μL of Lipofectamine MessengerMAX reagent (Thermo Fisher Scientific) in Opti-MEM. RNA–lipid complexes were added dropwise to the cells, and genomic DNA was extracted 48 h post-transfection without fluorescence-based enrichment.

DNA extraction and indel efficiency analysis

For plasmid-transfected cells, approximately 10,000 mCherry-positive cells were collected by FACS and lysed in 20 μL of lysis buffer containing proteinase K at 55 °C for 30 min, followed by incubation at 95 °C for 5 min. For RNA-transfected cells, genomic DNA was extracted directly from harvested cells. For *in vivo* gene-editing analysis, genomic DNA was extracted from mouse tissues. For targeted amplicon sequencing, genomic regions flanking

the editing target sites were amplified by nested PCR with primers carrying sample-specific barcodes. The PCR products were pooled and purified for amplicon sequencing. Libraries were sequenced on the Illumina NovaSeq 6000 platform. Indel frequencies were quantified using CRISPResso2 (ref. 43). Refer to Supplementary Table 3 for information on the target site sequence and primers.

Analysis of Cas-OFFinder-predicted off-target sites

Candidate off-target sites for each tigRNA were identified using Cas-OFFinder[44] against the human reference genome (hg38), allowing up to two mismatches and no DNA or RNA bulges within the 18-nt target sequence. No limit was placed on the number of candidate sites returned. All candidate off-target sites meeting these criteria were selected for validation by targeted amplicon sequencing. PCR amplification, sequencing, and indel quantification were performed as described above. All predicted off-target site sequences and their corresponding primers are provided in Supplementary Table 4.

Animals

All animal experiments were approved by the Executive Committee on Laboratory Animal Management and Ethical Review at Northwest A&F University (Approval No. NWAFU-DK2025066). Mice were housed in a controlled barrier facility at 18–23 ˚C and 40–60% humidity under a 12-h light/dark cycle, with food and water available ad libitum. Eight-week-old B6D2F1 females were used as zygote donors, 8-week-old pseudopregnant ICR females as embryo recipients, and 6-week-old male C57BL/6 mice for AAV- and LNP-mediated *in vivo* editing.

Zygote microinjection and embryo transplantation

ParTasR mRNA was generated by *in vitro* transcription from a linearized template and purified by LiCl precipitation, and chemically synthesized tigRNA was obtained from GenScript. Before microinjection, the mixture of ParTasR mRNA and *PCSK9*-tigRNA was centrifuged for 10 min at 18,000×g and 4 ˚C, and the supernatant was then transferred to 0.2-mL RNA-free PCR tubes for injection.

Superovulated 8-week-old B6D2F1 females were mated with B6D2F1 males, and fertilized zygotes were collected from the oviducts 21 h after human chorionic gonadotropin administration. The mixture of ParTasR mRNA (100 ng/μL) and *PCSK9*-tigRNA (50 ng/μL) was injected into the cytoplasm of fertilized eggs in a droplet of M2 medium using a FemtoJet microinjector (Eppendorf) with constant flow settings. Injected zygotes were

cultured in M16 medium supplemented with amino acids at 37 ℃ under 5% CO_2 until the two-cell stage. Approximately 25 two-cell embryos were then transferred into the oviducts of pseudopregnant 8-week-old ICR females at 0.5 days post-coitum.

AAV8 production and *in vivo* delivery

AAV8 vectors carrying the ParTasR expression cassette and its cognate tigRNA cassette were produced by PackGene. Vector titers were quantified by qPCR with primers targeting the ITR region. Purified AAV8 vectors were stored at −80 ˚C until use.

For *in vivo PCSK9* editing, 6-week-old C57BL/6 mice received a single tail-vein injection of AAV8-ParTasR-tigRNA at a dose of 5×10^{13} viral genomes per kg. Livers were harvested at the indicated time points after injection, and genomic DNA was extracted for quantification of editing efficiencies by targeted amplicon sequencing as described above. Blood samples were collected before injection and on days 7, 14, 21, 28, 35, 49, and 63 after injection. Serum was collected to measure PCSK9 protein and LDL-C levels.

LNP formulation and *in vivo* delivery

An organic phase was prepared by dissolving ALC-0315, DSPC, cholesterol and ALC-0159 in ethanol at a predetermined molar ratio. Separately, ParTasR mRNA and *PCSK9*-tigRNA were diluted in 50 mM sodium acetate buffer to prepare the aqueous phase. The organic and aqueous phases were then combined at a 3:1 volume ratio to form LNPs. The resulting LNPs were buffer-exchanged against PBS and concentrated by ultrafiltration through a 30-kDa molecular-weight cut-off (MWCO) membrane. Encapsulation efficiency and RNA concentration were determined with the Quant-iT RiboGreen RNA assay kit according to the manufacturer's instructions. Particle size distribution and polydispersity index of the LNPs were determined by dynamic light scattering.

For *in vivo* delivery, LNPs were diluted in sterile PBS to the indicated dose based on the measured RNA concentration. Mice were assigned to treatment groups with three animals per group. Approximately 1 h prior to LNP administration, mice received dexamethasone intraperitoneally at 10 mg/kg in a volume of 10 mL/kg. On day 0, mice received a single intravenous injection of LNPs via the tail vein at the indicated doses in a volume of 10 mL/kg. Six days later, mice were euthanized and liver tissues were harvested for immediate genomic DNA extraction. Editing efficiency at the mouse *PCSK9* locus was determined by targeted amplicon sequencing as described above.

Histology and immunofluorescence

Paraffin-embedded mouse liver sections were deparaffinized in xylene and rehydrated through a graded ethanol series. Antigen retrieval was performed in EDTA antigen-retrieval buffer (pH 9.0) by microwave heating. After cooling to room temperature, sections were washed three times in PBS and blocked with 3% hydrogen peroxide for 25 min in the dark. Sections were then blocked with 3% BSA for 30 min at room temperature, followed by overnight incubation at 4 °C with a mouse anti-PCSK9 primary antibody (HUABIO, EM1701-26; 1:300). After three washes in PBS, sections were incubated for 50 min at room temperature with an HRP-conjugated goat anti-mouse secondary antibody (Servicebio, GB23301; 1:100). PCSK9 signal was visualized with CY5-Tyramide reagent (Servicebio, G1232; 1:500) for 10 min. Nuclei were counterstained with DAPI for 10 min, and sections were mounted in antifade mounting medium. Fluorescence images were acquired using a digital slide scanner.

Statistics and reproducibility

The DMS sequencing data were analyzed by BWA[45] and SAMtools[46]. The NGS data of indel were analyzed by CRISPResso2 (ref. 43). The predicted structures of ParTasR nucleases were generated by using AlphaFold3 (ref. 40), and visualized in UCSF ChimeraX[42]. For deep mutational scanning of the ParTasR and tigRNA libraries, each sublibrary was screened in three independent replicates. To assess reproducibility among replicates, we calculated Spearman's rank correlation coefficients between the Log_2 fold-change (Log_2FC) values of all variants for each pairwise comparison. Data are presented as mean ± s.e.m. unless otherwise indicated. Values below the lower limit of quantification (LLOQ) of the ELISA were set to 0 for calculating mean values and percentage reductions. Comparisons between two groups were performed using unpaired, two-tailed *Student's t*-tests. Comparisons among multiple groups were performed by one-way or two-way ANOVA followed by Tukey's or Dunnett's post-hoc tests for multiple comparisons, as appropriate. Indel frequencies across the 24 target sites were compared among WT-ParTasR, PIVOT, and SpRY by one-way repeated-measures ANOVA (blocked by target site) and Dunnett's post-hoc test. Statistical significance is indicated as $^{*}p < 0.05$, $^{**}p < 0.01$, $^{***}p < 0.001$; ns, $p \geq 0.05$. No statistical methods were used to predetermine sample size; sample sizes were instead chosen on the basis of standards in the field to ensure adequate statistical power. All attempts at replication were successful, and no data were excluded from the analyses. For animal studies, mice were

randomly assigned to treatment groups, and all injections and phenotype assessments were performed in a blinded manner where feasible.

Data availability

Next-generation sequencing data are available at the National Center for Biotechnology Information (NCBI) Sequence Read Archive database under the BioProject accession code PRJNA1513783. Source data are provided with this paper.

References

40. Abramson, J. et al. Accurate structure prediction of biomolecular interactions with AlphaFold 3. *Nature* **630**, 493–500 (2024).
41. Emsley, P., Lohkamp, B., Scott, W.G. & Cowtan, K. Features and development of Coot. *Acta Crystallogr. D Biol. Crystallogr.* **66**, 486–501 (2010).
42. Pettersen, E.F. et al. UCSF chimera-A visualization system for exploratory research and analysis. *J. Comput. Chem.* **25**, 1605–1612 (2004).
43. Clement, K. et al. CRISPResso2 provides accurate and rapid genome editing sequence analysis. *Nat. Biotechnol.* **37**, 224–226 (2019).
44. Bae, S., Park, J. & Kim, J.S. Cas-OFFinder: a fast and versatile algorithm that searches for potential off-target sites of Cas9 RNA-guided endonucleases. *Bioinformatics* **30**, 1473–1475 (2014).
45. Li, H. & Durbin, R. Fast and accurate short read alignment with Burrows-Wheeler transform. *Bioinformatics* **25**, 1754-1760 (2009).
46. Danecek, P. et al. Twelve years of SAMtools and BCFtools. *Gigascience* **10**, giab008 (2021).

Acknowledgments

We appreciate the support from the Gene Editing Scientific Teaching (NWAFU-GEST), High-Performance Computing (HPC), and Life Science Research Core Service platforms (KR Huang, XR Liu, L Chen, M Zhou, and LQ Li) at Northwest A&F University (NWAFU). The authors also wish to express their gratitude to the members of Castalysis Bioscience (Shanghai) Co., Ltd. for their contributions in supplying experimental materials and insightful discussions. This work is supported by the Biological Breeding-Major Projects (2023ZD04074 to K.X.), the National Natural Science Foundation of China (32673659, 32441080 to Y.W., and 32630098 to X.W.), the National Science and Technology Major

Project of China (2023ZD0500501 to Z.W.), the Shanghai Committee of Science and Technology (26J32800301 to Z.W.), the Young Elite Scientists Sponsorship Program (2024QNRC001 to Z.W.), the Shaanxi Provincial Science and Technology Innovation Team (2025RS-CXTD-059 to X.W.) and local grants (2024A02004-1, 2025NC-YBXM-109, QCYRCXM-2023-104 to Y.W., and 2023A02011-2 to X.W.).

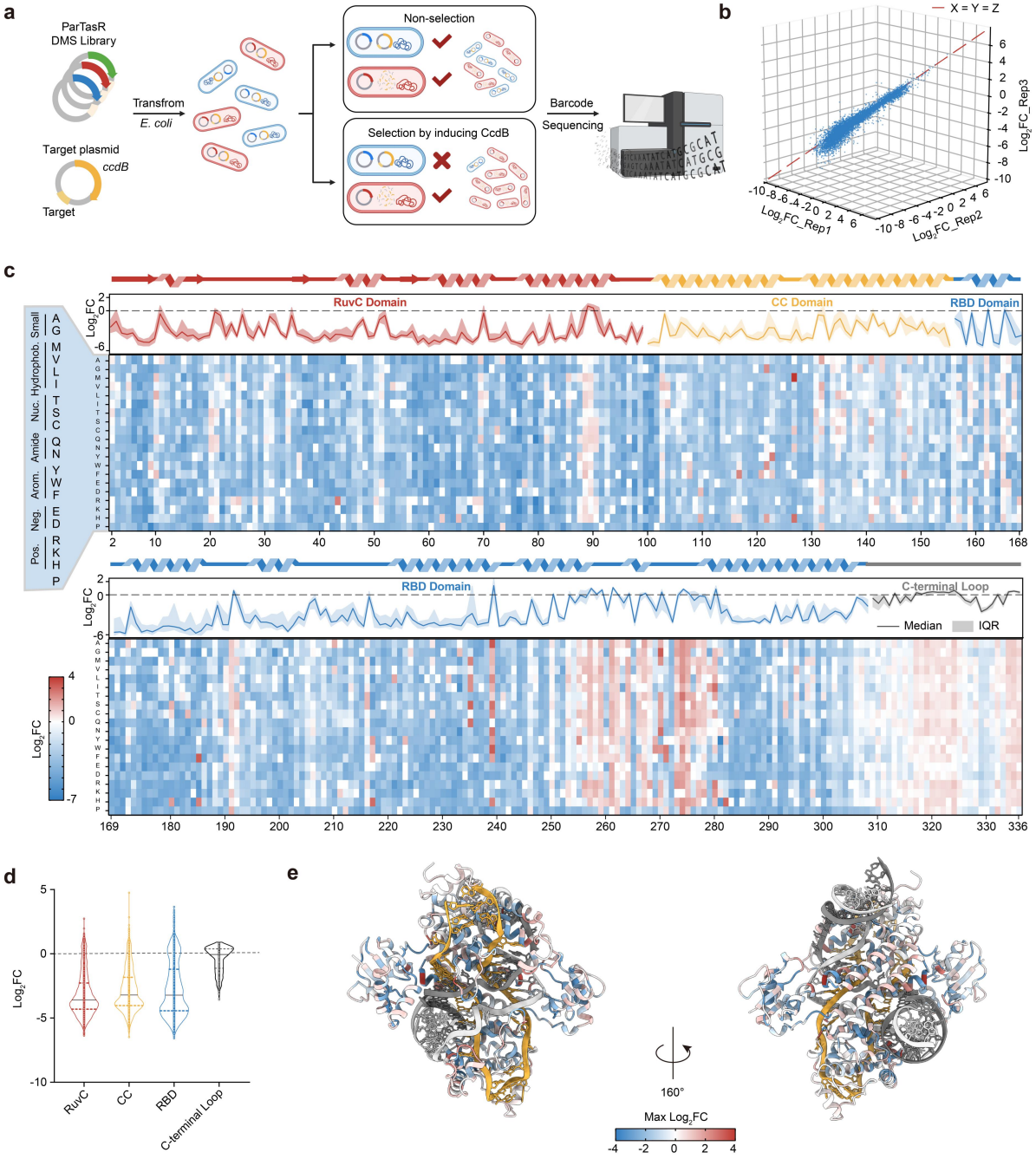
Author contributions

Y.W. and Z.W.W. conceived the project. Y.W., Z.W.W., K.X. and Y.L. designed the experiments. K.X., Y.L., P.W. and S.L. performed data analysis. Z.W.W., Y.L. and Y.G. conducted the structural prediction assays. Y.L., P.W., Z.C., Y.C. and Y.Q. performed the deep mutational scanning experiments in *Escherichia coli.* S.L., Z.M.W., Q.K., Z.H. and R.F. performed cell transfection and FACS. P.W., Y.L., X.C. and Z.M. performed animal experiments. Y.W., Z.W.W. and Y.L. wrote the manuscripts. Y.W., Z.W.W., X.W., K.X. and Y.L.C. supervised the project.

Competing interests

The authors declare no competing interests.

608 **Figures**



609

610 **Fig. 1 | Deep mutational scanning of the ParTasR protein identifies mutations that**
611 **increase activity. a,** Schematic of the cleavage-dependent *ccdB* counterselection assay used
612 for deep mutational scanning (DMS) of full-length ParTasR in *E. coli.* Active variants cleave
613 the *ccdB*-containing plasmid, allowing cell survival under selection. **b,** Reproducibility of the
614 enrichment profiles across three independent screens. **c,** Heat map of the mean Log_2FC
615 values for all single-amino-acid substitutions across ParTasR. Columns indicate residue
616 positions and rows the substituted amino acids; the overlaid line shows the median Log_2FC at
617 each position, and the shaded region the interquartile range. **d,** Distribution of Log_2FC values

for single-amino-acid substitutions across the indicated ParTasR domains. Each point represents one substitution; violin plots show the distribution within each domain. **e,** Enrichment scores projected onto the AlphaFold3-predicted ParTasR-tigRNA-DNA ternary complex.

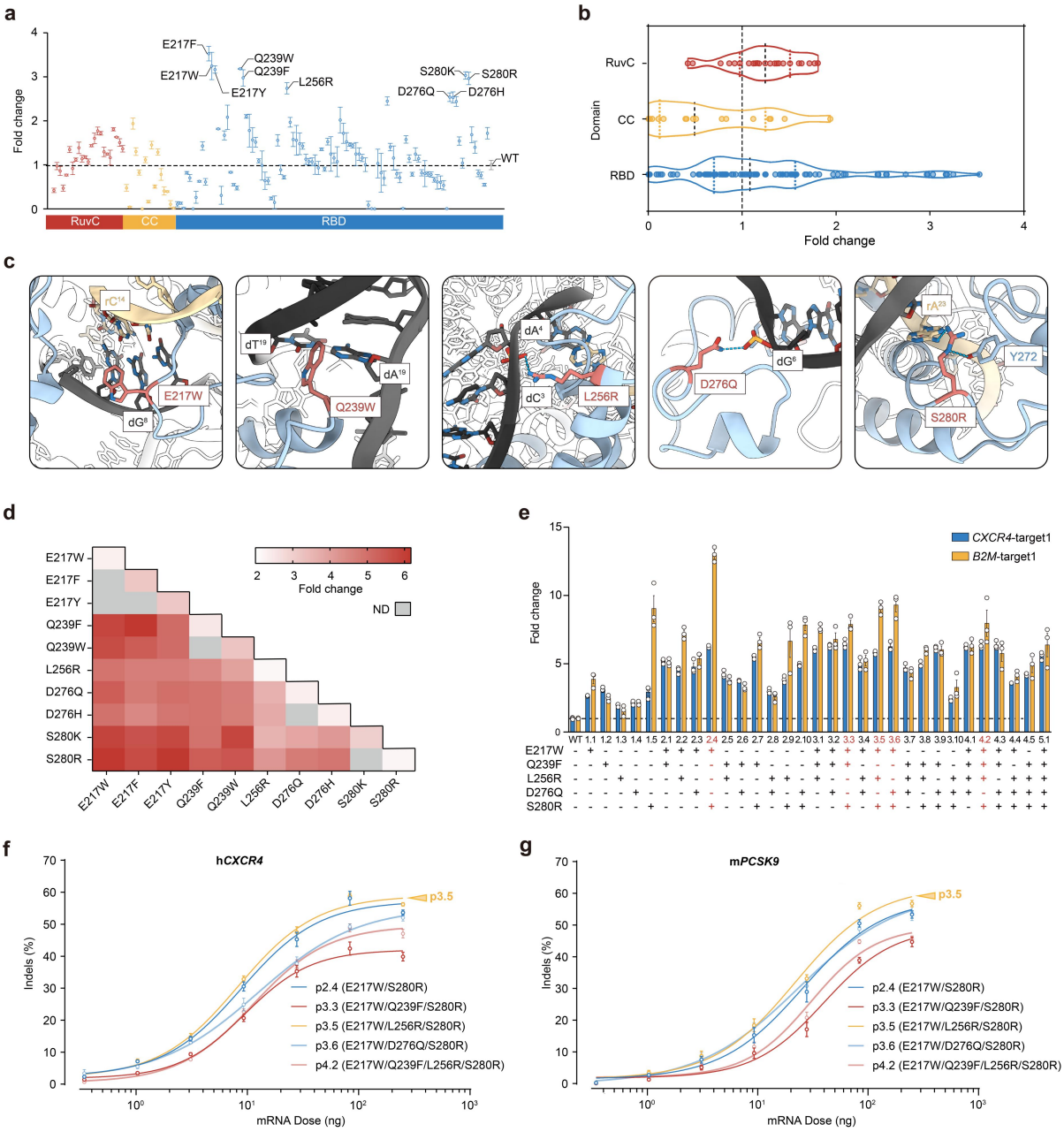


Fig. 2 | Combinatorial engineering transforms the fitness landscape into a hyperactive TIGR-ParTasR editor. a, Comprehensive evaluating of the 125 DMS-identified variants ($Log_2FC > 1$) by amino acid substitution in HEK293T cells. The dashed line indicates the cleavage activity of WT-ParTasR. **b,** Distribution of editing activities among single-amino-acid variants across the RuvC, coiled-coil (CC), and RNA-binding (RBD) domains. **c,** Predicted structures of representative top-performing substitutions. **d,** Pairwise assembly of the ten leading mutations at the *CXCR4* locus in HEK293T cells. Gray boxes indicate no available data (ND). **e,** Comparison of genome-editing efficiencies mediated by triple, quadruple, and quintuple combinatorial variants at the *CXCR4* and *B2M* loci in HEK293T cells. **f,g,** mRNA dose–response profiling of leading combinatorial variants at human *CXCR4*

(f) and mouse *PCSK9* **(g)** loci. Values and error bars are expressed as mean ± s.e.m. (n = 3 independent biological replicates). Fold-change is defined as the editing efficiency of ParTasR variants relative to WT-ParTasR.

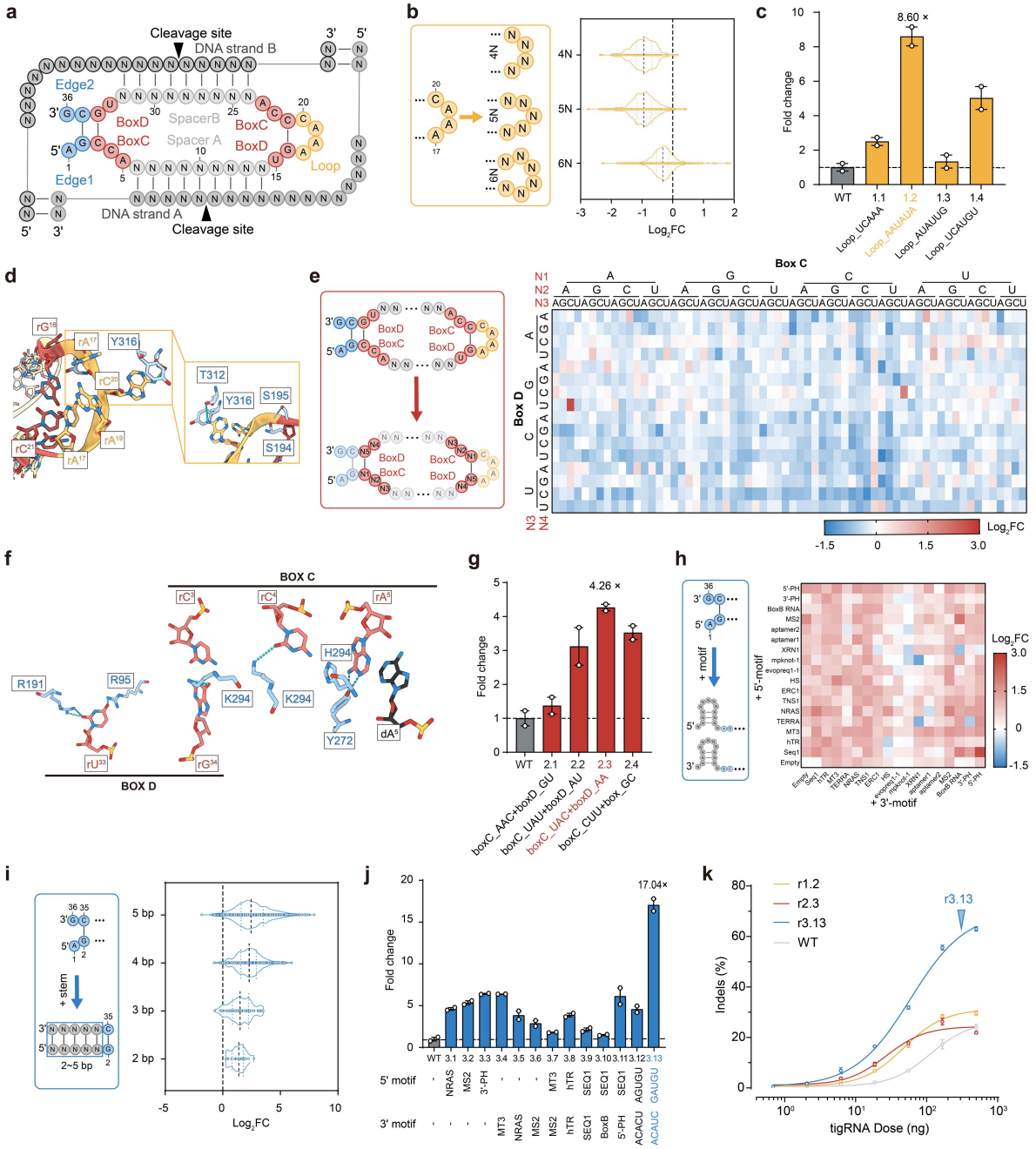


Fig. 3 | Profiling the TIGR-ParTasR tigRNA mutational landscape identifies gain-of-function mutations. a, Schematic of the tigRNA scaffold highlighting the loop, box C, box D, edge1, and edge2 regions subjected to module-focused mutagenesis. **b,** Screening of central loop libraries connecting boxC/boxD at lengths of 4, 5, and 6 nt. **c,** Genome-editing efficiencies of representative loop variants at the *CXCR4* locus following co-transfection ParTasR mRNA and corresponding tigRNA in HEK293T cells. **d,** Structural models of interactions between the central loop nucleotides and ParTasR. **e,** Heat map of enrichment scores from saturation mutagenesis of the boxC/boxD motifs. **f,** Structural models of interactions between boxC/boxD nucleotides and ParTasR. **g,** Genome-editing efficiencies of

representative boxC/boxD variants at the *CXCR4* locus in HEK293T cells. **h,i,** Heat map of enrichment scores for tigRNA variants with stabilizing motifs (**h**) and paired terminal stems (**i**). **j,** Genome-editing efficiencies of representative variants with stabilizing motifs and paired terminal stems at the *CXCR4* locus in HEK293T cells. **k,** Dose–response profiling of engineered tigRNA variants. Fold-change is defined as the editing efficiency of tigRNA variants relative to WT-tigRNA.

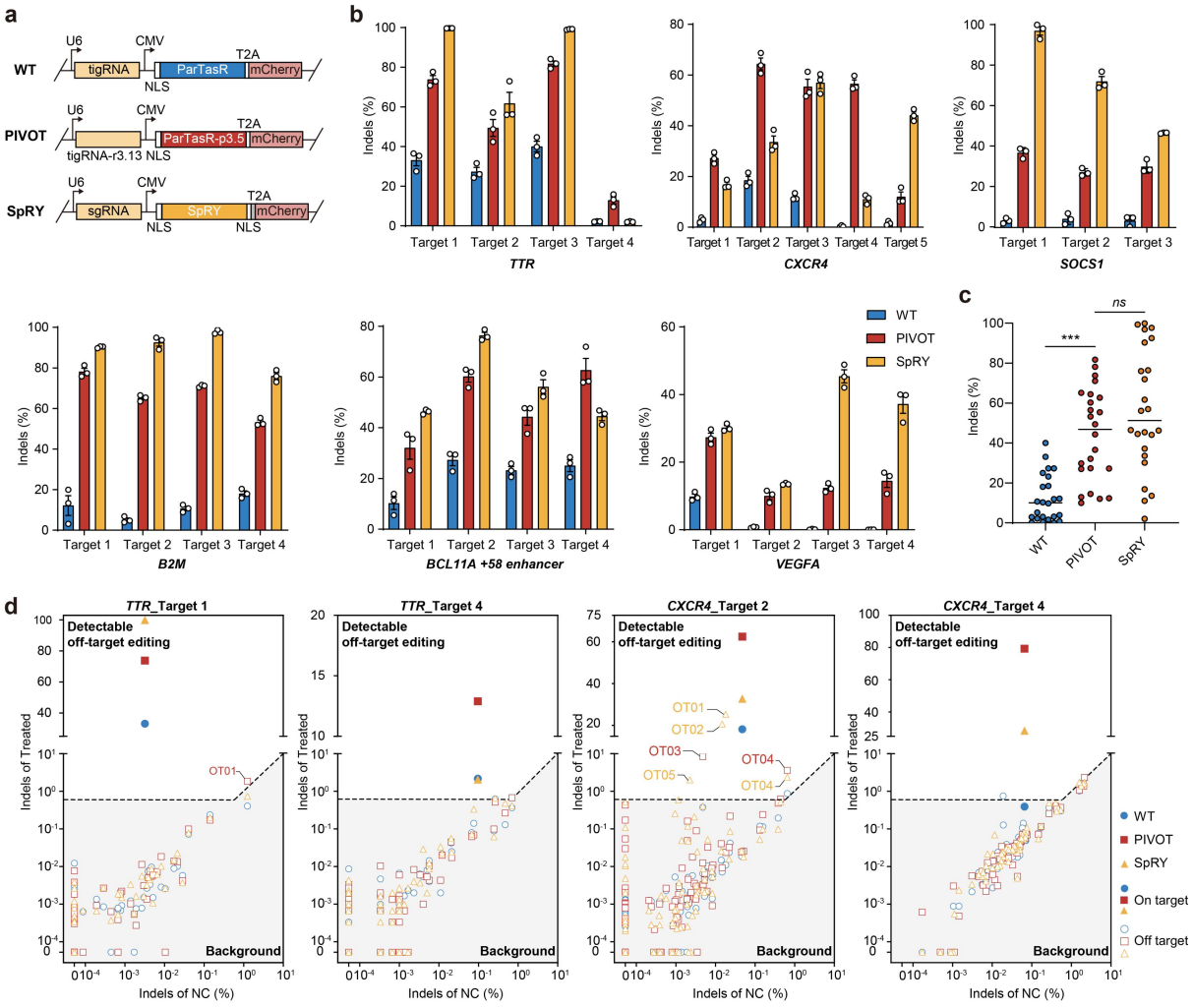


Fig. 4 | Comparison of genome-editing efficiency and specificity of the engineered PIVOT system and SpRY in human cells. a, Schematic of the wild-type ParTasR, PIVOT and SpRY systems. **b,** Genome-editing efficiency of wild-type ParTasR, PIVOT, and SpRY at 24 endogenous targets across six loci (*TTR*, *CXCR4*, *SOCS1*, *B2M*, *BCL11A*, and *VEGFA*) in HEK293T cells. **c,** Dot plot showing genome-editing activities of wild-type ParTasR, PIVOT, and SpRY. Each dot represents the mean editing efficiency of three independent biological replicates per endogenous locus. Asterisks indicate a significant increase in editing efficiency over WT-ParTasR-tigRNA by repeated-measures ANOVA (blocked by target site) and Dunnett's post-hoc test. $^{***}P \leq 0.001$; ns, not significant. **d,** On- and off-target analyses of wild-type ParTasR, PIVOT, and SpRY at four genomic loci (*TTR*-target1, *TTR*-target4, *CXCR4*-target2, and *CXCR4*-target4), with all off-target sites containing up to 2 mismatches as identified by Cas-OFFinder. Values and error bars are expressed as mean ± s.e.m. (n = 3 independent biological replicates).

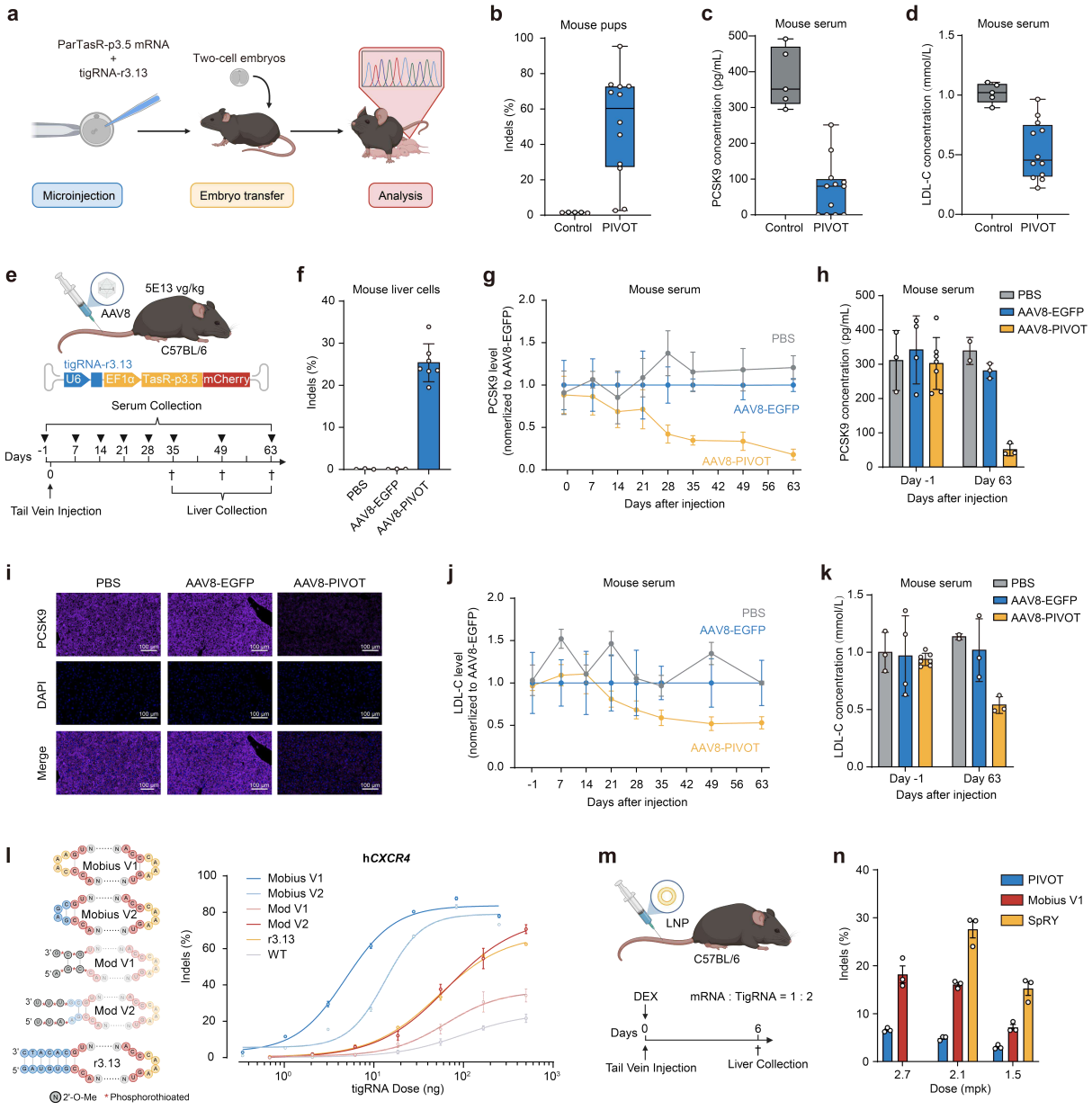


Fig. 5 | PIVOT/Mobius achieves efficient *in vivo* genome editing through microinjection, single AAV, or LNP delivery. a, Schematic of zygote microinjection with PIVOT targeting mouse *PCSK9*. **b,** Editing efficiency in mouse pups derived from injected zygotes. **c,d,** Detection of serum PCSK9 protein **(c)** and LDL-cholesterol (LDL-C) **(d)** levels in pups. **e,** Schematic of AAV8-mediated PIVOT delivery and sample collection timeline. **f,** Hepatic *PCSK9* editing efficiency at day 63 following AAV8-mediated delivery of PIVOT. **g,** Longitudinal serum PCSK9 protein levels following AAV8 administration. **h,** Absolute serum PCSK9 concentrations at baseline (day -1) and at endpoint (day 63). **i,** Representative immunofluorescence images of hepatic PCSK9 expression at day 63 after tail-vein injection of PBS, AAV8-PIVOT, or AAV8-EGFP. Scale bar: 100 μm. **j,** Longitudinal serum LDL-C levels following AAV8 administration. **k,** Absolute serum LDL-C concentrations at baseline

(day -1) and at endpoint (day 63). **l,** Dose–response profiling of circular, chemically modified, and linear tigRNA variants. **m,** Schematic of LNP-mediated delivery. **n,** Liver *PCSK9* editing efficiency following LNP delivery of PIVOT or PIVOT/Mobius at the indicated doses. Values and error bars are expressed as mean ± SEM ($n \geq 3$ independent biological replicates). Each dot represents an individual mouse for panels **b-d**, **f**, **h**, **k**, and **n**.

Supplementary Files

This is a list of supplementary files associated with this preprint. Click to download.

- SupplementaryInformation.pdf